Improvements in Shortwave Bulk Scattering and Absorption Models for the Remote Sensing of Ice Clouds

BRYAN A. BAUM,* PING YANG,+ ANDREW J. HEYMSFIELD,# CARL G. SCHMITT,# YU XIE,+ AARON BANSEMER,# YONG-XIANG HU,@ AND ZHIBO ZHANG&

* *Space Science and Engineering Center, University of Wisconsin—Madison, Madison, Wisconsin*
+ *Texas A&M University, College Station, Texas*
# *National Center for Atmospheric Research,** Boulder, Colorado*
@ *NASA Langley Research Center, Hampton, Virginia*
& *Goddard Earth Sciences and Technology Center, University of Maryland, Baltimore County, Baltimore, Maryland*

(Manuscript received 2 August 2010, in final form 8 November 2010)

ABSTRACT

This study summarizes recent improvements in the development of bulk scattering/absorption models at solar wavelengths. The approach combines microphysical measurements from various field campaigns with single-scattering properties for nine habits including droxtals, plates, solid/hollow columns, solid/hollow bullet rosettes, and several types of aggregates. Microphysical measurements are incorporated from a number of recent field campaigns in both the Northern and Southern Hemisphere. A set of 12 815 particle size distributions is used for which $T_{cld} \leq -40°C$. The ice water content in the microphysical data spans six orders of magnitude. For evaluation, a library of ice-particle single-scattering properties is employed for 101 wavelengths between 0.4 and 2.24 μm. The library includes the full phase matrix as well as properties for smooth, moderately roughened, and severely roughened particles. Habit mixtures are developed for generalized cirrus, midlatitude cirrus, and deep tropical convection. The single-scattering properties are integrated over particle size and wavelength using an assumed habit mixture to develop bulk scattering and absorption properties. In comparison with global Cloud Aerosol Lidar with Orthogonal Polarization (CALIOP) data, models built with severely roughened particles compare best for all habit mixtures. The assumption of smooth particles provided the largest departure from CALIOP measurements. The use of roughened rather than smooth particles to infer optical thickness and effective diameter from satellite imagery such as the Moderate Resolution Imaging Spectroradiometer (MODIS) will result in a decrease in optical thickness and an increase in particle size.

1. Introduction

To infer and intercompare the microphysical and optical properties of ice clouds from the current suite of spaceborne sensors that compose the National Aeronautics and Space Administration (NASA) Earth Observing System, the bulk single-scattering properties of the ice clouds must be described in a consistent fashion from the visible (VIS: $0.4 < \lambda < 0.75$ μm) through the infrared (IR: $5 < \lambda < 15$ μm) spectral region. The models need to encompass the passive radiometric measurements from the Moderate Resolution Imaging Spectroradiometer (MODIS; Platnick et al. 2003), along-track solar spectral measurements from the Multiangle Imaging Spectroradiometer (MISR; Diner et al. 1998), polarization measurements provided by the Polarization and Directionality of the Earth Reflectance (POLDER; Deschamps et al. 1994) sensor, hyperspectral IR measurements from the Atmospheric Infrared Sounder (AIRS; Aumann et al. 2003), and active measurements from the Cloud–Aerosol Lidar with Orthogonal Polarization (CALIOP) on the *Cloud Aerosol Lidar and Infrared Pathfinder Satellite Observations* (*CALIPSO*; Winker et al. 2010) platform. Much has been learned

** The National Center for Atmospheric Research is sponsored by the National Science Foundation.

Corresponding author address: Dr. Bryan A. Baum, SSEC, University of Wisconsin—Madison, 1225 W. Dayton St., Madison, WI 53706.
E-mail: bryan.baum@ssec.wisc.edu

DOI: 10.1175/2010JAMC2608.1

from intercomparison studies to date, with the resulting refinement of bulk ice-cloud scattering models for solar wavelengths described in this study.

The development of ice-cloud bulk scattering models will not end with current sensors. Future instrumentation will extend the spectral domain of measurements from the ultraviolet through the far IR. Multispectral polarization measurements at selected wavelengths from the VIS through shortwave IR (SWIR: $0.75 < \lambda < 3$ μm) were to be provided by the Aerosol Polarimetry Sensor as part of the Glory mission (Mishchenko et al. 2007), which was lost in a launch failure in March 2011. Future models will need to extend from the ultraviolet (UV: $0.28 < \lambda < 0.4$ μm) through the far IR ($15 < \lambda < 100$ μm) regimes and also be able to include the full phase matrix for polarization measurements.

The development of more realistic ice-cloud bulk scattering models will lead to improvements in our capability of representing ice clouds in the general circulation models (GCMs) and thereby improve our understanding of the role of ice clouds in the climate system. Ice-cloud parameterization schemes in the current generation of GCMs are generally based on a limited description of ice-particle microphysical and optical properties. Our bulk scattering models, which will eventually cover the spectrum from UV through far IR, can be readily used for the development of an ice-cloud parameterization scheme suitable for application in GCMs. Moreover, a GCM ice-cloud parameterization scheme based on our model will be consistent with what is widely used in satellite cloud products and will facilitate intercomparison between model simulations and remote sensing products.

The basic method to build bulk ice-cloud scattering and absorption models was reported in Baum et al. (2005a,b; 2007). These models incorporated microphysical data from a variety of field campaigns (Baum et al. 2005a) and databases of ice-particle single-scattering properties developed from several different numerical light-scattering models. The development of band models was described for a narrowband imager such as MODIS (Baum et al. 2005b) that required consideration of the imager spectral response functions. These models were used for MODIS collection-5 cloud products. The differences between the collection-4 and collection-5 (hereinafter C4 and C5, respectively) cloud microphysical and optical properties were investigated by Yang et al. (2007).

Spectral models have been developed using a similar approach for use by hyperspectral IR sensors (Baum et al. 2007) as well as for the shortwave region (Kindel et al. 2010). Models developed for a generic set of Advanced Very High Resolution Radiometer channels are being used in operational cloud-property retrievals (Heidinger and Pavolonis 2009) by the National Oceanographic and Atmospheric Administration. These models enable intercomparison studies to be performed that implement internally consistent ice-cloud bulk scattering properties.

As these ice-cloud models are percolating through the community, users are providing feedback and criticism. In the shortwave spectral region, for example, it was noted that there are discontinuities in certain properties such as the absorption efficiency over the particle size range. Additional limitations include gaps in spectral coverage, the use of only smooth-faced particles in the scattering calculations, a lack of microphysical data for ice clouds having ice water content (IWC) values below 10^{-3} g m^{-3} (which tend to have very small effective diameters), and an issue with the interpretation of two-dimensional cloud (2D-C) probe data when large ice particles shatter at the inlet to the probe, leading to unrealistically large numbers of small particles (Field et al. 2006). One issue that caused considerable confusion to users of the models was in how to most appropriately treat the delta-transmission energy term in radiative transfer calculations.

This study addresses the issues that have come to the attention of the authors and describes the research advances that have been made since the previous studies were published. Because the basic approach to building the bulk scattering-property models is similar to the earlier studies, we will focus on the improvements. Section 2 describes the data used in this study, including microphysical data from recent field campaigns and active lidar measurements from CALIOP. Section 3 describes the many changes in the derivation of ice-particle single-scattering properties as well as the implementation of two new habits: the hollow bullet rosette and the aggregate of plates. Section 4 discusses the derivation of more realistic habit mixtures than that used in the earlier studies and discusses the microphysical and single-scattering properties that result from their adoption. This discussion makes use of CALIOP measurements. The implications of the new models for the remote sensing of ice clouds are discussed in section 5.

2. Data

a. Microphysical data

The ice-cloud bulk scattering models described in Baum et al. (2005a) were developed from 1117 individual particle size distributions (PSD) obtained from midlatitude and tropical field campaigns. The PSDs provide a description of particle number density from approximately 50 to >6000 μm and were developed primarily from 2D imaging probe data; data from small-particle probes for <50 μm were not used because of issues related to shattering of large ice on the inlets of

TABLE 1. Number of particle size distributions for each field campaign. The total sample set has been filtered by the requirement that the cloud temperature be colder than −40°C. A total of 12 815 PSDs are used in this study. Here, CPI is cloud particle imager; 2D-P is two-dimensional precipitation probe; CAPS is cloud, aerosol, and precipitation spectrometer; and CIP is cloud-imaging probe.

Field campaign	Location	No. of 5-s-avg PSDs $T_{cld} \leq -40$°C	Probes
ARM IOP	Oklahoma	1420	2D-C, 2D-P, CPI
TRMM KWAJEX	Kwajalein, Marshall Islands	201	2D-C, 2D-P, CPI
CRYSTAL-FACE	Caribbean Sea	62	CAPS, VIPS
SCOUT	Darwin, Australia	553	FSSP, CIP
ACTIVE—Monsoons	Darwin	4268	CAPS
ACTIVE—Squall lines	Darwin	740	CAPS
ACTIVE—Hectors	Darwin	2583	CAPS
MidCiX	Oklahoma	2968	CAPS, VIPS
PreAVE	Houston, TX	20	VIPS

these probes. Each of the PSDs from the in situ data came with additional information, including the measured cloud temperature T_{cld}, IWC inferred from a mass–dimensional relationship being applied to the measured PSD or calculated from the set of 1117 PSDs, and median mass diameter D_m. For this set of PSDs, the IWC ranged from 10^{-3} to 10^{0} g m^{-3} and the cloud temperatures ranged from −25° to −76°C. As shown in Baum et al. (2005a), the effective diameter D_{eff} tended to increase monotonically with IWC, and the smallest D_{eff} that could be developed from this set of PSDs was 30 μm.

One problem encountered during the development of the MODIS C5 models was that the bulk scattering models used in MODIS C4 were based on a set of 12 PSDs consisting of either four or five size bins, with no particles having a maximum diameter of >700 μm. A few of the C4 models had very small D_{eff} values as a result of not including large particles in the PSDs. To develop C5 models that had smaller D_{eff} values, a sensitivity study was conducted in which the number of the smallest particles in a set of PSDs was increased by a factor of 100 or 1000 to account for the absence of particles below 50 μm in the measurements. This artificial increase in small particles resulted in D_{eff} values as small as 10 μm. Thus the C5 models had D_{eff} values that ranged from 10 to 180 μm.

In the current study, data are now incorporated from a number of recent field campaigns as shown in Table 1. The number of PSDs available for use has increased by more than an order of magnitude, from 1117 to 12 815, even when filtering the available data using the homogeneous freezing temperature (i.e., $T_{cld} \leq -40$°C). The IWC now ranges from 10^{-6} to 10^{0} g m^{-3}, an increase of three orders of magnitude from the Baum et al. (2005a) study. The IWC is obtained by applying an improved mass–dimensional relationship to each PSD as discussed in Heymsfield et al. (2010).

The number concentration of small particles that may be present in a given PSD has received much scrutiny in recent years. The question arises as to how many of the small particles are caused by large particles shattering at the inlet to the 2D-C (and similar) probe. Microphysical data have been reprocessed to mitigate the shattering issue for the 2D probes as described by Field et al. (2006) from the Atmospheric Radiation Measurement Program (ARM) intensive observation period (IOP) near Lamont, Oklahoma; Tropical Rainfall Measuring Mission (TRMM) validation flights conducted at Kwajalein, Marshall Islands (KWAJEX); and the Cirrus Regional Study of Tropical Anvils and Cirrus Layers–Florida-Area Cirrus Experiment (CRYSTAL–FACE) campaigns. As shown in Table 1, new data have been provided from the Pre-*Aura* Validation Experiment (PreAVE; 2004), the Midlatitude Cirrus Experiment (MidCiX; 2004), and the Stratospheric-Climate Links with Emphasis on the Upper Troposphere and Lower Stratosphere (SCOUT) campaign held in November–December 2005 in Darwin, Australia. For SCOUT, the targeted ice clouds were in the upper troposphere and lower stratosphere (de Reus et al. 2009). The PSD data were obtained from a Forward Scattering Spectrometer Probe (FSSP). Because of the absence of particles of sizes of several hundred micrometers and above in the very high altitude clouds sampled during SCOUT, data from the small-particle probes were less subject to shattered-particle artifacts. The SCOUT data are from eight flights and span the temperature range from −30° to −86°C. Also from Darwin are microphysical data obtained during the Aerosol and Chemical Transport in Tropical Convection (ACTIVE) campaign in Darwin from November 2005 to February 2006. For ACTIVE, anvil cirrus were sampled at temperatures from −31° to −66°C from regimes that included premonsoon, monsoon, and localized convection events such as a daily thunderstorm that forms over the Tiwi Islands near Darwin during the wet season that is so consistent it has been given the name ''Hector.''

The National Center for Atmospheric Research Video Ice Particle Sampler (VIPS) probe is used to

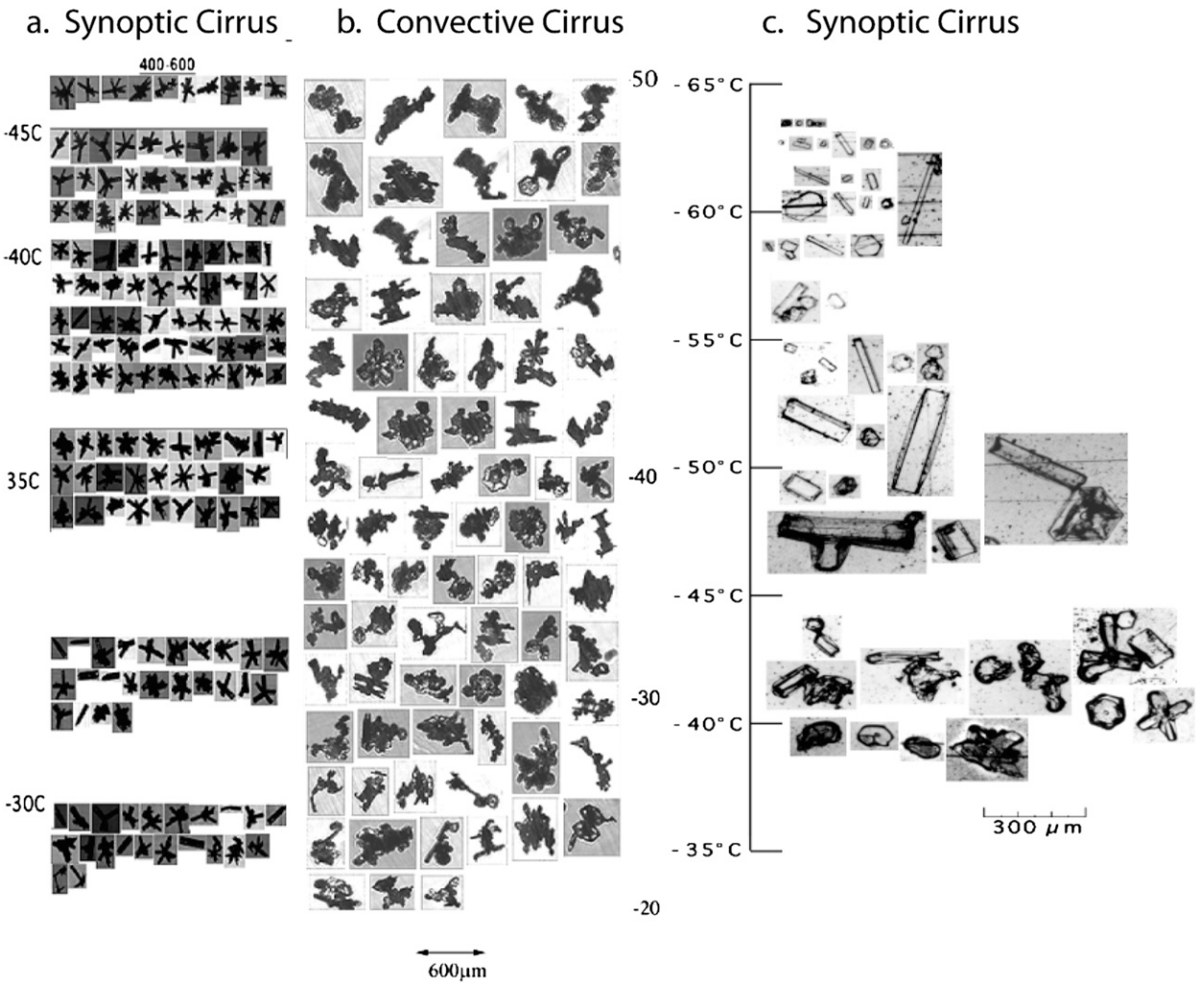

FIG. 1. Ice-particle images show (a) bullet rosettes as the predominant habit at all heights in synoptic cirrus, (b) complex habits in tropical deep convection, and (c) pristine habits in synoptic cirrus.

obtain particle-size data down to sizes of about 10 μm. The VIPS probe does not have the same shattering issue that other small-particle probes may have, although the collection tape can get covered over when IWC values are high, limiting the measurements to IWC of $<$0.02–0.03 g m^{-3}. Based on these new data, models can be built for much lower D_{eff} values without artificially increasing the number of small particles.

Droplets associated with temperatures near -40°C and below tend to be small when they freeze (Heymsfield and Miloshevich 1995). For ice particles that form from homogeneous nucleation, the bigger the initial liquid water drop is, the more likely it is to grow as a polycrystal (e.g., the 3D bullet rosette). An example of synoptically generated cirrus with bullet rosettes as the predominant habit is shown in Fig. 1a. Particles that develop in the strong updrafts of deep tropical convection (Fig. 1b) can be very different than those formed via homogeneous nucleation (Fig. 1a) or in cold-topped synoptic cirrus (Fig. 1c). Ice clouds that form in deep tropical convection tend to be associated with much higher IWC values and therefore higher volume extinction coefficients. Figure 2 shows the aircraft lidar penetration distance into ice clouds from different flight tracks from synoptic cirrus and tropical convection. For the lidar, the signal becomes attenuated for clouds that are optically thick ($\tau \geq 3$, where τ is optical thickness). This figure shows the cloud boundaries observed by the aircraft (solid circles) and the penetration distance from cloud top that is observed by a lidar. When $\tau = 3$ in this figure, an arrow is placed on the vertical bar. For synoptic ice clouds the lidar generally penetrated very deeply into the cloud layer, whereas for deep tropical cirrus the lidar signal can attenuate very close to cloud top.

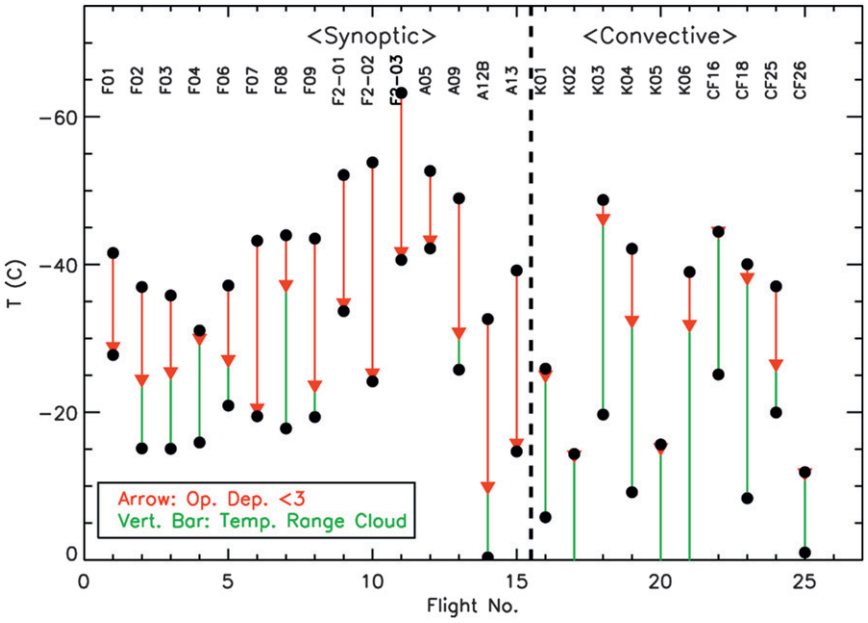

FIG. 2. Aircraft lidar penetration distance into ice clouds from different flight tracks from synoptic cirrus (left of dotted line) and tropical convective ice clouds (right of dotted line).

b. *CALIOP*/CALIPSO

CALIPSO flies in formation with NASA's Earth Observing System *Aqua* platform and is part of the A-Train suite of sensors. CALIOP provides 532-nm cross-polarization and 1064-nm observations. A general introduction to polarization may be found in Liou (1992). The quantity P_{11} is estimated from the layer-integrated attenuated backscatter γ' of ice clouds that are optically thick. Platt (1979) and Platt and Dilley (1981) provide a description of the various equations relating to the calculation of optical properties from lidar measurements. These studies provide a relationship between γ' and the backscatter-to-extinction ratio and hence to the normalized scattering phase function at 180°:

$$P_{11}(\Theta = 180^\circ) = 4\pi \frac{2\eta\gamma'}{1 - \exp(-2\eta\tau)}, \tag{1}$$

where τ is cloud optical thickness and η is the multiple-scattering factor. The quantity η accounts for the effective reduction in the ice-cloud optical thickness that is due to multiple scattering within the lidar beam. With the assumption of $\eta = 0.45$ and $\tau \geq 3$, $P_{11}(\Theta = 180^\circ) \sim 3.6\pi\gamma'$. The linear depolarization ratio δ is estimated from the ratio of the perpendicular backscatter to the parallel backscatter for a given wavelength (Hu 2007; Hu et al. 2009). For a single backscattering event, the associated depolarization ratio is

$$\delta = \frac{P_{11} - P_{22}}{P_{11} + P_{22}}, \tag{2}$$

which can be rearranged to provide P_{22}/P_{11}:

$$\frac{P_{22}}{P_{11}} = \frac{1 - \delta}{1 + \delta}. \tag{3}$$

Although $P_{11} = P_{22}$ for spherical particles (so that $P_{22}/P_{11} = 1$), P_{22}/P_{11} will depart from a value of 1 with increasing nonsphericity. In this sense, P_{22}/P_{11} is an indicator of particle nonsphericity (Mishchenko et al. 2002). For this study, a full year (2008) of CALIOP data from the 5-km level-2 cloud product was analyzed to study the statistics of P_{11} and P_{22}/P_{11} at $\Theta = 180^\circ$. Because ice clouds with horizontally oriented particles may contaminate the P_{11} and P_{22} statistics, they were filtered from the dataset by applying the cloud-phase algorithm of Hu et al. (2009) to the level-2 cloud backscatter data. As a result, this study focuses on ice clouds with randomly oriented particles.

3. Improvements in ice-particle single-scattering properties

Previous work was based on two different extensive libraries of the microphysical and single-scattering properties that were developed for a variety of ice-crystal habits, including droxtals (Yang et al. 2003; Zhang et al.

2004), three-dimensional bullet rosettes, solid and hollow columns, plates, and aggregates (Yang et al. 2000). A droxtal is a quasi-spherical particle with 20 facets. The aggregate of solid columns was the only roughened particle [the degree of surface roughness denoted by $\sigma = 0.5$ was used, following the method of Yang et al. (2008a)]; the other habits have smooth facets for which $\sigma = 0$. One of these databases covered solar wavelengths, although there were some spectral gaps. These gaps must be filled to make full use of data from sensors such as the solar spectral flux radiometer (Kindel et al. 2010). These gaps also prevented the development of complete broadband models for use in shortwave radiance/flux calculations and GCM parameterization schemes. The other database covered the wavelength spectrum from medium-wave infrared (MWIR: $3 < \lambda < 8$ μm) to far-IR. In addition, some aspects (e.g., ice-particle aspect ratios) of the earlier databases were not consistent over the solar and infrared spectral regions. In this section, we detail modifications to the derivation of ice-particle single-scattering properties that address these limitations.

a. Ice refractive index

Earlier calculations of single-scattering properties at solar wavelengths employed the complex refractive indices of ice in Warren (1984) for wavelengths below 1.4 μm while those of Gosse et al. (1995) were used for wavelengths greater than 1.4 μm. The Gosse et al. (1995) refractive indices deviated from data published by Warren (1984) by as much as 60% at some wavelengths. The complex refractive index of ice from the ultraviolet to the microwave regions has been updated in Warren and Brandt (2008). The real part of the index of refraction changes primarily only in the far IR, but there are significant differences in the imaginary part of the index of refraction in various spectral regions from the ultraviolet to the far IR. This latest compilation is now used in the scattering property computations.

b. New habits

Based on inspection of detailed ice-particle imagery as in Fig. 1, three new habits were developed: a hollow bullet rosette, a ''small'' aggregate of plates, and a ''large'' aggregate of plates. A hollow bullet rosette particle is one in which the individual bullets have cavities. A bullet is an individual branch of a rosette that is characterized as a hexagonal column with a hexagonal pyramidal tip; a rosette is composed of multiple bullets attached to a common nucleus. Properties of a hollow bullet rosette particle are described in Schmitt et al. (2006), Schmitt and Heymsfield (2007), and Yang et al. (2008b).

The aggregate of solid columns adopted in Baum et al. (2005a) is a very compact particle with a much higher volume-per-length relationship than the other particles have. The aggregate of solid columns may be an unrealistic depiction of the large particles found in ice clouds formed by convection such as tropical anvil cirrus. The model of Westbrook et al. (2004) supports adoption of a spatial aggregate. Furthermore, analysis of in situ microphysical data suggests that large particles have less mass than is suggested by this aggregate of solid columns. The mass–dimensional aspects of the aggregates are discussed in Schmitt and Heymsfield (2010).

This finding raises an issue about the adoption of a more realistic habit for these large particles. An aggregate of bullet rosettes has been suggested by Um and McFarquhar (2007), whereas other studies suggest an aggregate of plates (Evans et al. 2005; Um and McFarquhar 2009; Heymsfield et al. 2002). One issue is whether such particles tend to form as a spatial, rather than compact, aggregate. Baran (2009) showed that the asymmetry parameter is the same for a three-plate spatial aggregate as it is for a six-plate spatial aggregate. This result suggests that, with spatial aggregates, multiple reflections between plates are insufficient to decrease the asymmetry parameter as much as happens with compact aggregation (Um and McFarquhar 2009).

Based on images of ice aggregates, a spatial (rather than compact) aggregate of plate particle was chosen for further development with one caveat: no individual plate could be more than 700 μm in maximum dimension. This limitation, based on in situ observations, led to the development of two different types of particles involving aggregates of plates as shown in Fig. 3. The small aggregate of plates (Fig. 3a) is composed of five individual plates and is used to represent particles having a maximum dimension of less than about 1200 μm. The large aggregate of plates (Fig. 3b) is composed of more individual plates and is used to represent particles from 800 to 10 000 μm in maximum dimension. The scattering properties of an individual aggregate were computed using the discrete dipole approximation (DDA) for particles having a small size parameter (defined as the ratio of the particle circumference to the incident wavelength) or an improved geometric optics method (IGOM) for particles having a large size parameter (Xie et al. 2011). Computations were performed for five different realizations of the small and large particle as shown in Fig. 3. The results were subsequently averaged to form a composite set of single-scattering properties at each particle size and wavelength.

On the basis of the new habits, there is now a set of nine different habits available for use in single-scattering computations: droxtals, plates, solid/hollow bullet rosettes, solid/hollow columns, aggregates of solid columns, and small/large aggregates of plates. The ice-particle volume

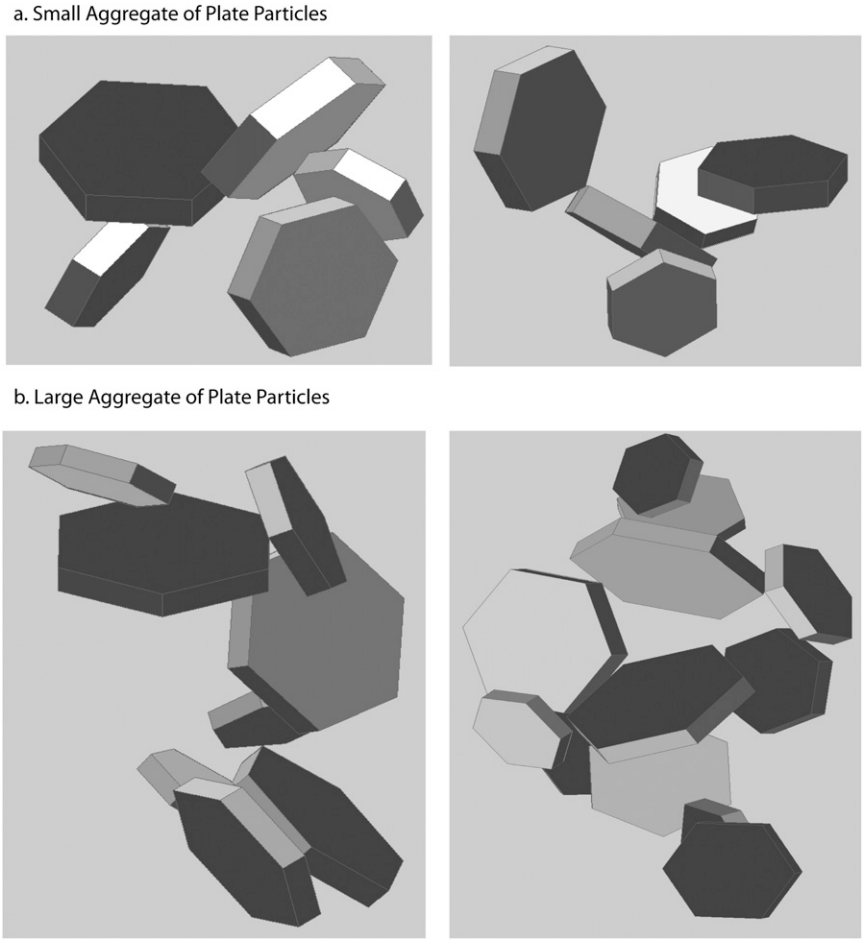

FIG. 3. (a) ''Small'' aggregates of plates composed of up to five individual plates wherein no individual plate has a maximum dimension of >700 μm. This particle is used in a habit mixture for particles having a maximum dimension of <1200 μm. (b) ''Large'' aggregate of plates composed of a minimum of seven individual plates wherein no individual plate has a maximum dimension of >700 μm. The large particle is used in a habit mixture for particles having a maximum dimension of >800 μm.

for each of these habits as a function of maximum dimension D_{max} is given in Fig. 4.

c. *Improvements in the scattering models*

Enhancements to the IGOM are discussed in Bi et al. (2009); a brief summary is provided here. In previous calculations, use of the IGOM for smooth particles led to a δ-transmission term f_δ at VIS-to-SWIR wavelengths. The f_δ term represents the fraction of energy that passes through parallel facets of an ice particle (such as a plate) without scattering (i.e., at a scattering angle of 0°). As such, this energy must be accounted for when performing radiative transfer calculations. This contribution is different from the strong forward peak in the scattering phase function at solar wavelengths that includes the effect of diffraction. However, f_δ is actually a numerical artifact of the IGOM that results from how the near field is mapped to the far field. With a new treatment of forward scattering that more rigorously maps the near field to the far field to account for the ray spreading effect, there is no longer an f_δ term. One result from this improvement is that the asymmetry factor now accounts for the energy in the forward peak more accurately.

Another issue noted in the previous models is that the absorption and extinction efficiencies in previous calculations displayed some small discontinuities when making the transition from the Rayleigh to geometric-optics regimes, in the so-called resonant region. This transition region ranges from approximately 20 to 50 in size parameter values. Part of the discontinuity was due to the treatment of above-edge effects as noted by

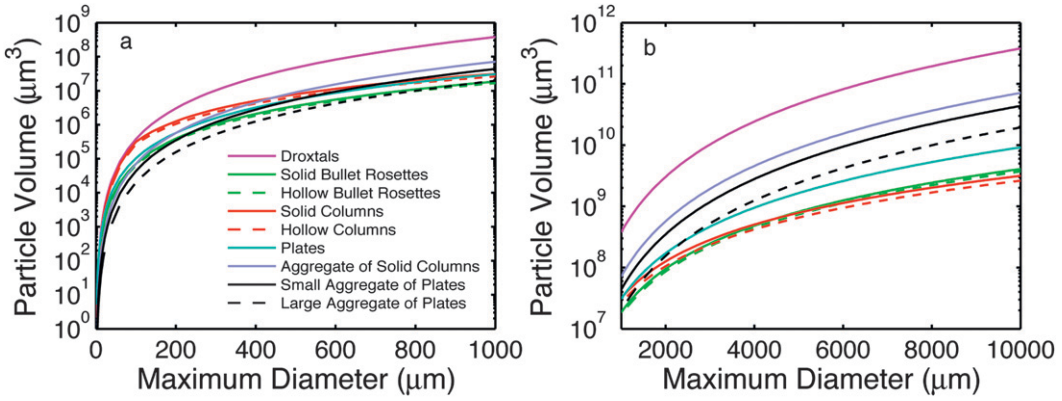

FIG. 4. Ice-particle volume as a function of habit and maximum dimension D_{max} for (a) $D_{max} \leq 1000$ μm (small- to moderately sized particles) and (b) $D_{max} > 1000$ μm (moderate to large particles).

Mitchell et al. (2001). By improving the treatment of particle edge effects, there is now a smooth transition of the scattering efficiency between the IGOM and a rigorous numerical method [e.g., the finite-difference time-domain or DDA techniques; Mishchenko et al. (2000) and references cited therein].

d. Ice-particle surface roughness

Yang et al. (2008a) discussed two different ray-tracing methods to treat ice-particle surface roughness in the geometric-optics regime. One method involves a rigorous treatment in which the surface of a particle contains multiple small ''roughness facets'' and then considers external reflections between the roughness facets and potential reentries of outgoing rays back into the particle. The second method involves an approximate approach that simply perturbs the normal to the particle surface for each reflection–refraction event without considering further facet interactions as in the more rigorous approach. This study indicated that the approximate algorithm accounts sufficiently for surface roughness in calculating the single-scattering properties. As such, the approximate algorithm is used in the calculation of the new database of single-scattering properties.

In addition to creating a database for the various habits that have completely smooth surfaces, two different values are assumed for the surface roughness. Moderately roughened particles assume $\sigma = 0.03$, and a value of $\sigma = 0.5$ is assumed for severely roughened particles. The values chosen for the roughness parameter may seem arbitrary. As shown in Baum et al. (2010), completely smooth hexagonal particles display halos at scattering angles of 22° and 46° in the forward scattering direction, as well as in the backscattering at 156° and 180°. With $\sigma = 0.03$, the only halo remaining is at 22°; otherwise the phase function is featureless. No halo features are present with a high degree of surface roughness (i.e., a large value of σ).

e. Library of solar single-scattering properties

The planned database of ice-particle single-scattering properties from the UV through the far IR is still under construction, but for this study a limited library of properties is employed for 101 wavelengths between 0.4 and 2.24 μm. The wavelengths were chosen to provide the spectral information necessary to build models for selected MODIS bands for testing prior to collection-6 software deliveries. The library includes the full phase matrix and properties for smooth, moderately roughened, and severely roughened particles ($\sigma = 0$, 0.03, and 0.5, respectively). Baum et al. (2010) discuss the effect of particle roughening on the phase matrix, showing in particular that P_{22}/P_{11} is especially sensitive to both habit and surface roughening in the backscattering ($\Theta = 180°$).

f. Comparison of recomputed and original MODIS C5 models

The MODIS C5 models were recomputed and compared with the original models to determine the impact of the changes—in particular, the effect of no longer having an f_δ term on the scattering phase function. Figure 5 shows an example of such a comparison for MODIS band 2 ($\lambda = 0.86$ μm) for $D_{eff} = 60$ μm. The phase function is shown in Fig. 5a for $10° \leq \Theta \leq 180°$ and in Fig. 5b (the insert) for $\Theta \leq 10°$. At forward scattering angles, the magnitude of the recomputed phase function (red line) is higher than that of the original, which is not unexpected since the scattered energy originally associated with f_δ has been spread out to small scattering angles. The opposite is true in the backscattering angles (i.e., the magnitude of the recomputed phase function is lower than that of the original). Also of note is that the oscillations evident in the original phase function at small scattering angles are

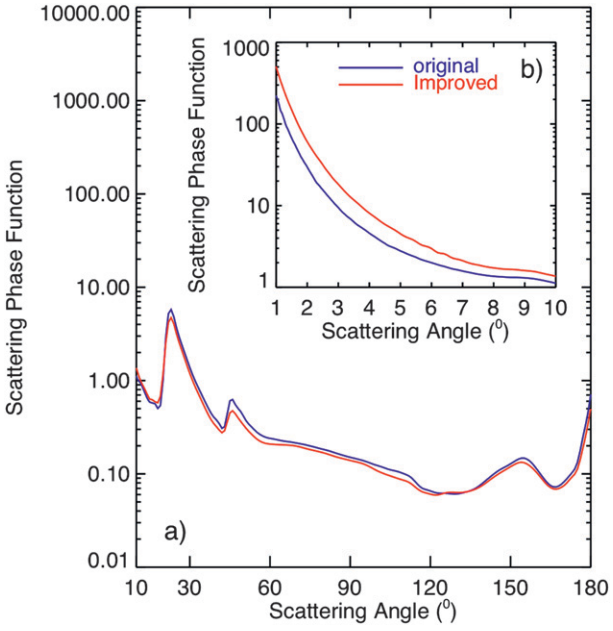

FIG. 5. The MODIS C5 scattering phase function for band 2 (λ = 0.86 μm) for the original model (blue line) and the recomputed model (red line) for $D_{\text{eff}} = 60$ μm for scattering angles (a) between 10° and 180° and (b) between 1° and 10°. At small scattering angles, the magnitude of the recomputed phase function is larger than that of the original. This is caused primarily by a new treatment of forward scattering implemented in IGOM. The recomputed phase function lacks the oscillations observed in the original model at small scattering angles. The new treatment of forward scattering has a negligible impact on the asymmetry factor *g,* with original and recomputed values of 0.833 and 0.827, respectively.

eliminated in the new model. However, the removal of f_δ has only negligible impact on the asymmetry factor g; the values for the original and recomputed models are 0.833 and 0.827, respectively.

4. Development of new habit mixtures and the implications for single-scattering properties

For the MODIS C5 models, Baum et al. (2005a) developed a habit mixture that minimized the differences between calculated and inferred (in situ) IWC and D_m values. Each PSD was divided into four particle size domains based on the maximum diameter D_{max}, which is the diameter of a circle that completely encloses the 2D image of a particle. The size domains were defined as follows: $D_{\text{max}} < 60$ μm, $60 < D_{\text{max}} < 1000$ μm, $1000 < D_{\text{max}} < 2000$ μm, and $D_{\text{max}} > 2000$ μm. Some restrictions were imposed on the individual habits. For example, droxtals were used for particles for which $D_{\text{max}} < 60$ μm. An upper limit on D_{max} for plates was imposed at 1000 μm, and an upper limit on D_{max} for both solid and hollow columns was imposed at 2000 μm. Aggregates were used only when $D_{\text{max}} > 1000$ μm, and solid bullet rosettes were used for all but the smallest particle sizes. Although this habit mixture incorporated all the habits available at that time for which we had computed single-scattering properties, the habit mixture changed abruptly when making the transition from one size domain to the next.

The challenge in developing a more physically realistic habit mixture is to take into account 1) the new habits, 2) a desire for the percentages of habits to change smoothly with D_{max}, 3) ice-particle surface roughness, and 4) polarization characteristics. For the ensuing discussion, results will be presented for three habit distributions. The first is a general habit mixture that uses all nine available habits as shown in Fig. 6a. The small aggregates of plates are used to represent particles having a maximum dimension of less than approximately 1200 μm, and the large aggregates of plates are used to represent particles from 800 to 10 000 μm. In the overlap region between 800 and 1200 μm, both small and large aggregates are employed. The second mixture uses the habits that are most appropriate for ice clouds that are not associated with tropical deep convective anvils (Fig. 6b); that is, it uses droxtals for small particles and neither small nor large aggregates of plates. The third mixture (Fig. 6c) is more appropriate for deep tropical convective anvils and implements solid columns rather than droxtals for small particles and aggregates of plates for the larger particles. Columns are used rather than droxtals for the smallest particles since high-altitude ice particles have been shown to be columnar in form (Heymsfield 1986). CALIOP measurements in the tropics include clouds at temperatures approaching −90°C, similar to the Heymsfield (1986) observations. The tropical habit distribution has a high concentration of plates at D_{max} between 50 and 500 μm. This may arguably not be the most realistic particle habit in this size range; a more realistically shaped particle would be an aggregate with a density somewhere between that of a droxtal and a plate.

As in Baum et al. (2005a), the bulk properties for each PSD are computed by integrating the individual habit properties over the size range using the assumed habit mixtures. Details are provided in the appendixes for the microphysical properties, spectral single-scattering properties at a given wavelength, and also the final integration of a given spectral response function. With this approach, the measured IWC and D_m values are compared in Fig. 7 with those computed using the full set of PSDs and the habit volumes as shown in Fig. 4. The comparison is shown in Fig. 7 for each of the three habit mixtures in Fig. 6. The desire is to derive habit mixtures that provide IWC and D_m values that compare

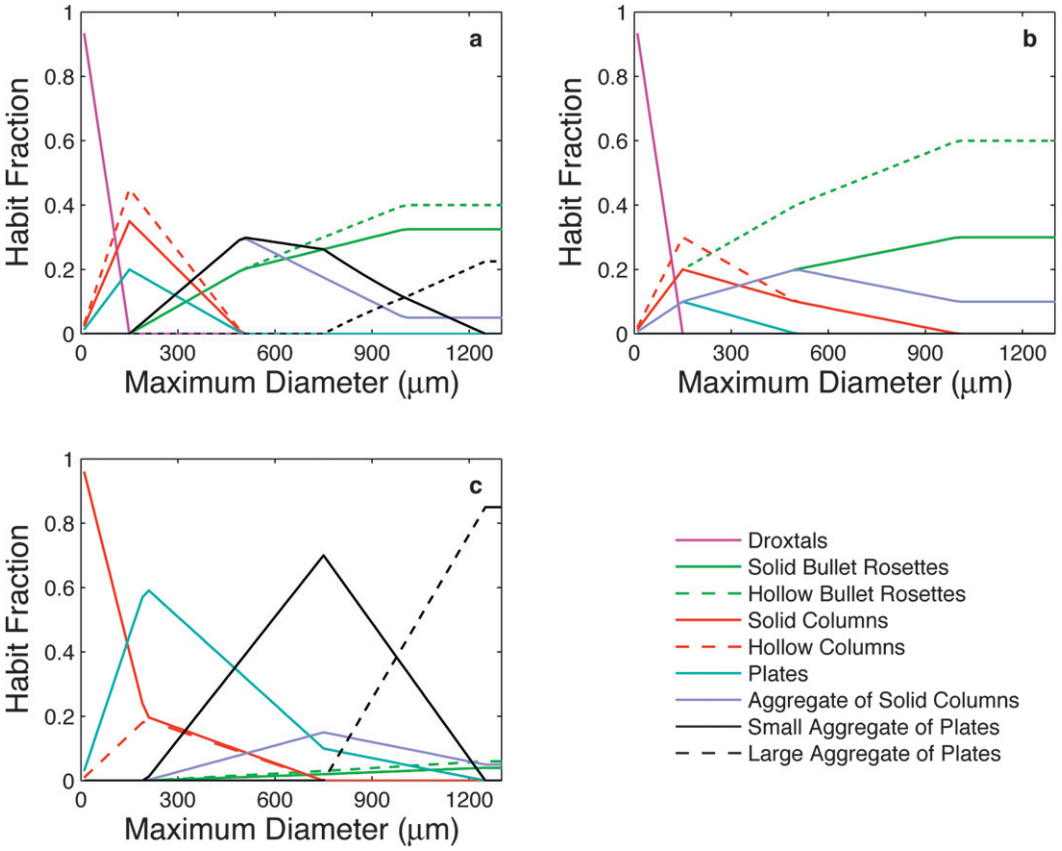

FIG. 6. Habit mixtures developed for use with the increased set of ice particles that include (a) a generalized mixture that is based on the full set of microphysical data regardless of cloud temperature, (b) a mixture that is based on microphysical data that have $-40° \geq T_{cld} \geq -60°C$ and that excludes aggregates of plates, and (c) a mixture for deep tropical convective ice clouds that excludes droxtals and that relies heavily on aggregates of plates.

reasonably well to those values provided from the in situ measurements. There is a small low bias in the computed D_m values for the generalized and midlatitude habit mixtures except at high values of D_m, and the computed tropical deep convection D_ms compare well to those from the in situ measurements except for values of D_m greater than about 350 μm. The measured IWC values have a low bias for all three habit mixtures. A higher-density aggregate type of particle in the 50- to 500-μm range would significantly increase the total mass in the size distributions, leading to closer agreement between the measured and calculated values. Future research will address the development of a more realistic habit in this size range.

Because the microphysical properties inferred from in situ data have their own associated uncertainties, and the potential combinations of ice habits are endless, the results in Fig. 7 seem to provide a reasonable comparison. However, the focus is on deriving a set of single-scattering properties appropriate for ice clouds, and a new constraint is provided by CALIOP data to provide guidance in assessing these habit mixtures. There is considerable variability of habits from one cloud to another, but we have tried to capture the habits in an average sense based on our in situ observations.

To compare with CALIOP data, P_{11} and P_{22}/P_{11} at $\Theta = 180°$ are calculated from the set of PSDs obtained from in situ data using the library of ice-habit single-scattering properties at a wavelength of 0.54 μm. A cloud temperature of $T_{cld} = -60°C$ is used to discriminate between deep tropical convective clouds and midlatitude clouds in the microphysical dataset. The bulk single-scattering properties are calculated for each PSD by using one of the habit mixtures shown in Fig. 6, thus providing the values of P_{11} and P_{22}/P_{11} at $\Theta = 180°$. Results of P_{11} and P_{22}/P_{11} at $\Theta = 180°$ from this approach are shown in Fig. 8 for CALIOP and the generalized habit mixture shown in Fig. 6a. The left column of panels (Figs. 8a,c,e,g) shows results for P_{11}, and the right column shows results for P_{22}/P_{11}. The top four panels show histograms on a log-10 scale based on a full year of CALIOP data from 2008 in the Northern Hemisphere as

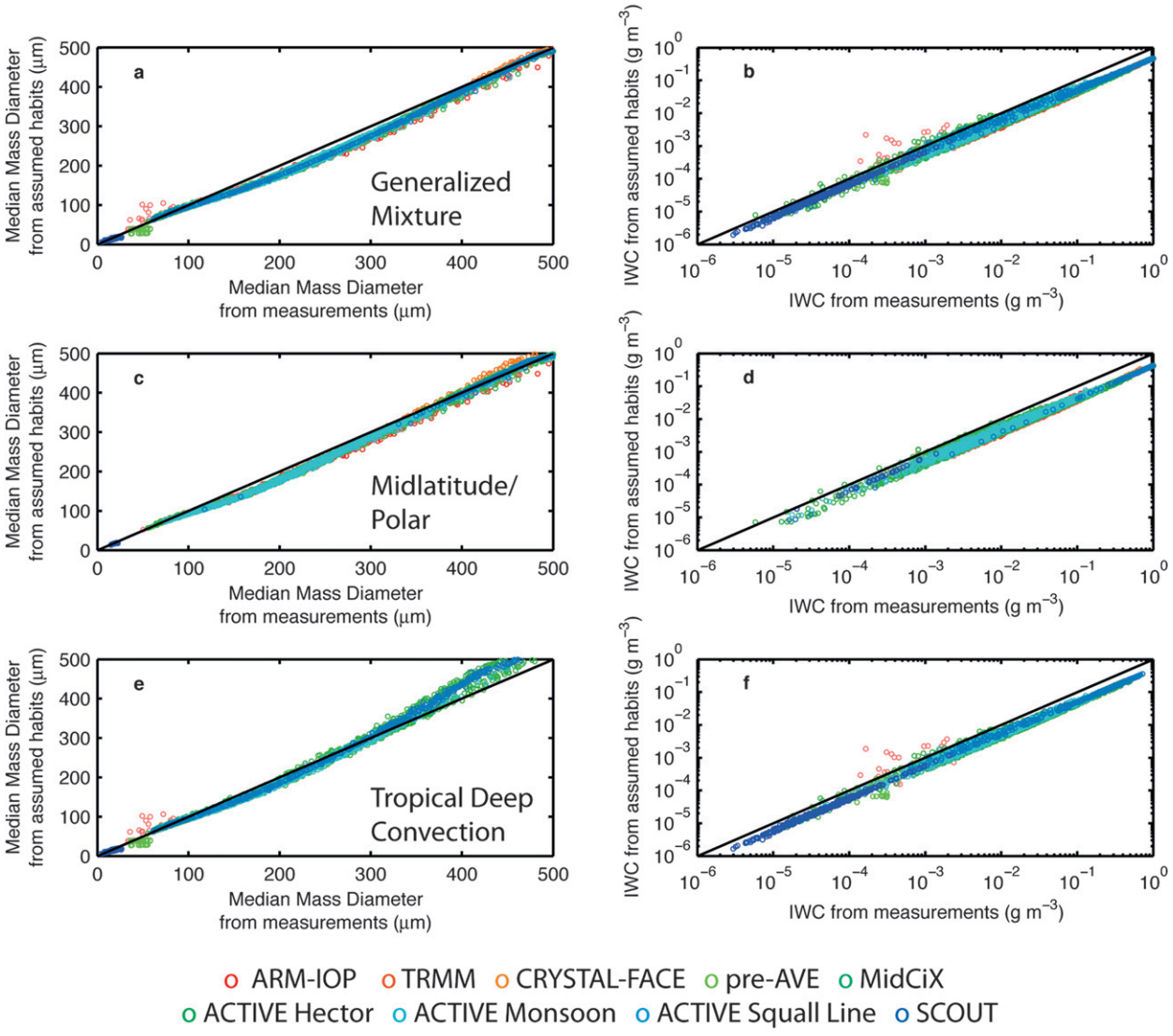

FIG. 7. For each of the size distributions obtained from the field campaigns listed in Table 1 in conjunction with the generalized habit mixture of Fig. 6a is shown a comparison of (a) in situ measurements (as inferred from mass–dimensional relationships) with calculated median mass diameter D_m and (b) measured with calculated IWC. (c),(d) As in (a) and (b), but for the midlatitude/polar (nontropical deep convection) ice-cloud habit mixture shown in Fig. 6b. (e),(f) As in (a) and (b), but using the tropical deep convection habit mixture shown in Fig. 6c.

a function of cloud temperature. The top two panels (Figs. 8a,b) show CALIOP data at latitudes of >30°N, and the second row shows results for the tropics (from 20°S to 20°N). For the CALIOP data, the values of P_{11} fall in a narrow range from 0.25 to 0.38 regardless of cloud temperature. The values of P_{22}/P_{11} range from 0.35 to 0.5 for the nontropical clouds (Fig. 8b), with a tendency to increase with decreasing cloud temperature; the values of P_{22}/P_{11} have a much smaller range for the tropical ice clouds. The bottom six panels show histograms based on the generalized habit mixture and the PSDs from the field campaigns for smooth (Figs. 8e,f), moderately roughened (Figs. 8g,h), and severely roughened particles (Figs. 8i,j). The range of P_{11} values for smooth particles is mostly larger than those from CALIOP. However, there are some outlying points at values of approximately 0.25. Most of these outlying data points come from the SCOUT mission that sampled extremely cold ice particles in the stratosphere. Since these data are heavily weighted toward small particles, these smaller values of P_{11} may be caused by the use of the droxtal habit. For the moderately and severely roughened particles, the P_{11} values are between 0.2 and 0.3, which is similar to the value predicted by the

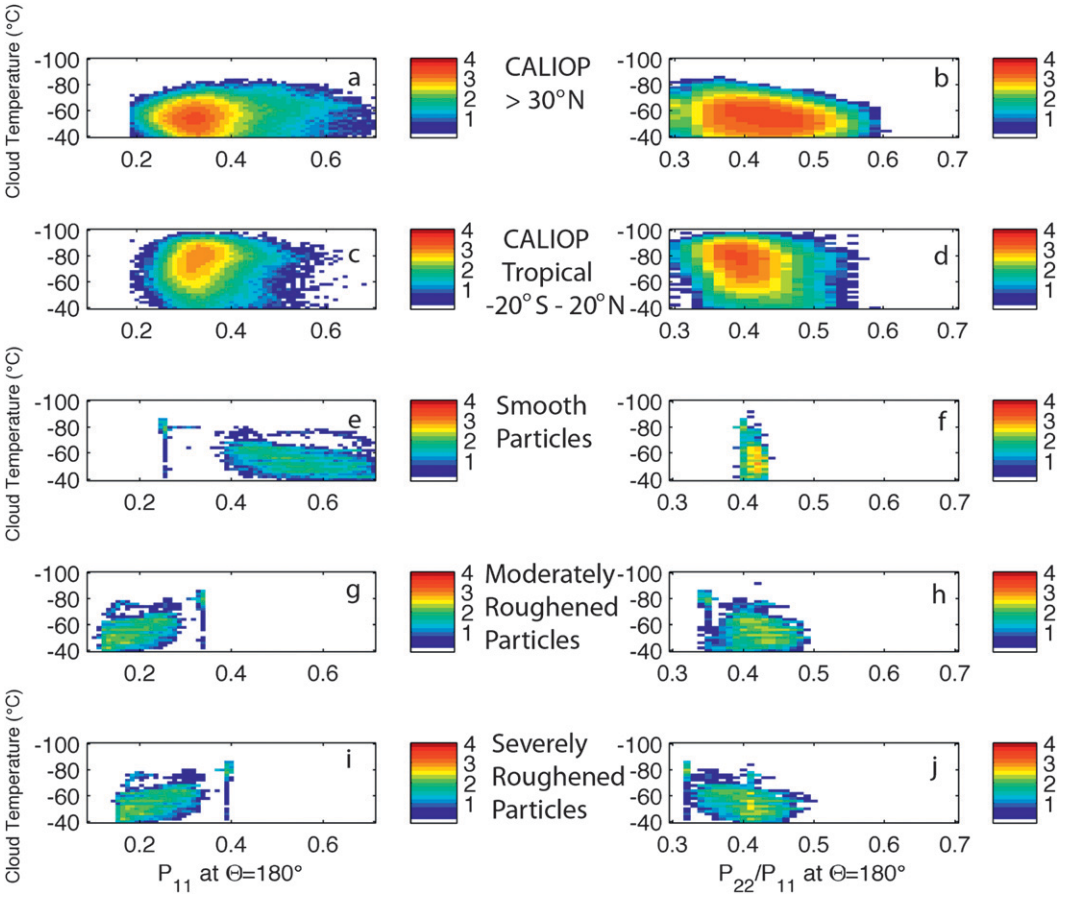

FIG. 8. The top four panels show histograms that are based on a full year of CALIOP data (2008) in the Northern Hemisphere of the temperature dependence of (a) P_{11} and (b) P_{22}/P_{11} at latitudes of >30°N and (c) P_{11} and (d) P_{22}/P_{11} in the tropics from −20°S to 20°N. The bottom six panels show histograms that are based on calculations involving the generalized habit mixture and the PSDs from the field campaigns for (e) P_{11} and (f) P_{22}/P_{11} for smooth particles, (g) P_{11} and (h) P_{22}/P_{11} for moderately roughened particles, and (i) P_{11} and (j) P_{22}/P_{11} using severely roughened particles. The color is in log-10 scale for all panels.

ensemble-model phase function discussed in Baran and Labonnote (2007), an analytic phase function (Baran et al. 2001), and the inhomogeneous hexagonal monocrystal phase function (Labonnote et al. 2001). These phase functions are all essentially featureless with no maxima, and the CALIOP data seem to support the backscattering values of P_{11} in these various featureless phase functions better than for smooth particles. The value assumed for the multiple-scattering factor is a topic of ongoing research.

The P_{22}/P_{11} values (Fig. 8f) fall within a very narrow range between 0.4 and 0.42. Neither P_{11} nor P_{22}/P_{11} as calculated assuming smooth particles captures the variability from CALIOP. At first glance, the results for both moderately roughened and severely roughened particles in the lowest four panels correspond well to the CALIOP results, but there are some interesting aspects that bear further discussion. The values for P_{11} seem to suggest a temperature dependence that is not evident in the CALIOP data. As in Fig. 8e for smooth particles, there are some outlier points at values of approximately 0.35 for moderately roughened particles (Fig. 8g) and 0.4 for severely roughened particles (Fig. 8i). Inspection of the P_{22}/P_{11} results for moderately roughened particles (Fig. 8h) does not indicate a strong temperature dependence, whereas results for severely roughened particles (Fig. 8j) suggest a weak dependence on temperature. The temperature dependence in the PSD-calculated P_{22}/P_{11} values could be a function of the depth within the cloud at which the measurements were made. The PSD measurements may come from optically thicker regions where the CALIOP measurements may not have been possible because of attenuation.

To explore the habit mixture further, results are shown in Fig. 9 using a set of habits (Fig. 6b) that excludes the particles found primarily in deep tropical

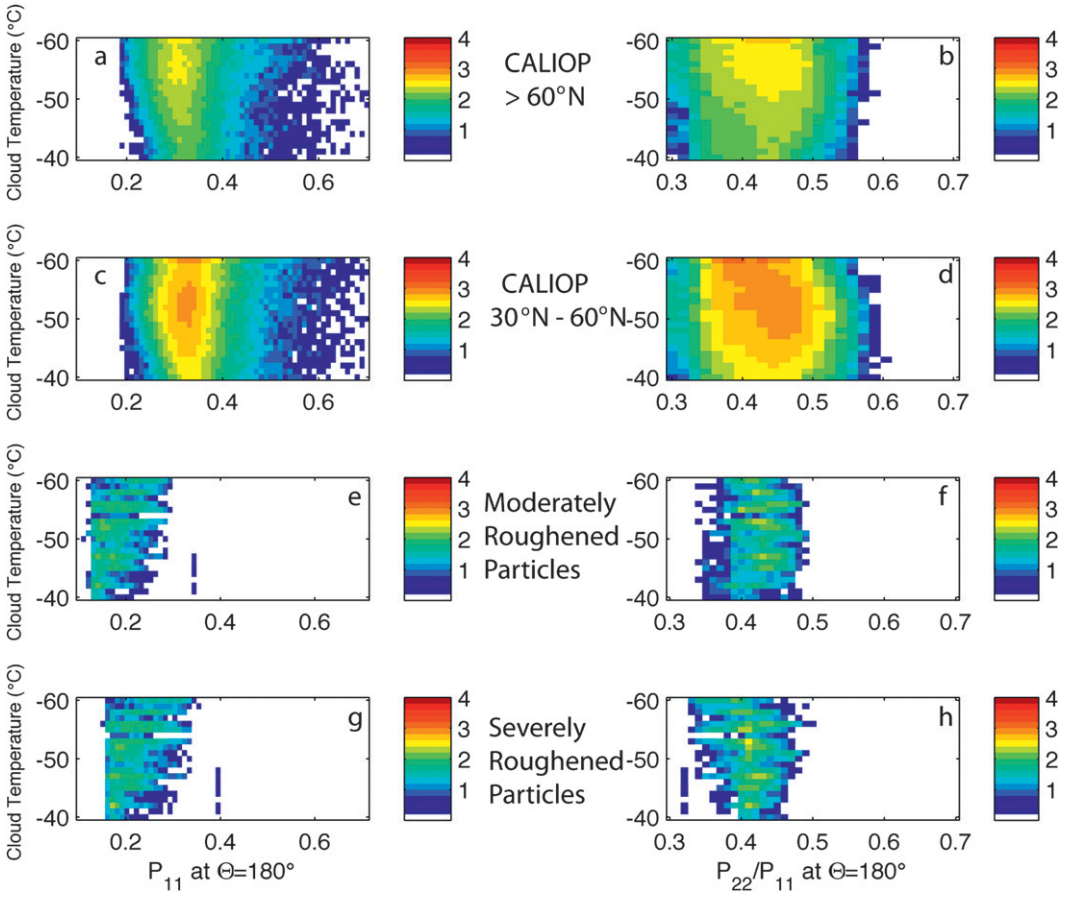

FIG. 9. As in Fig. 8, but for results that are based on the midlatitude/polar (nontropical deep convection) habit mixture shown in Fig. 6b. The microphysical data are filtered for $-40° \geq T_{cld} \geq -60°C$.

convective clouds (i.e., droxtals and aggregates of plates). Outside of the deep tropics, ice clouds generally have temperatures $T_{cld} \geq -60°C$, and therefore microphysical data are used in the bulk single-scattering calculations for which $-40° \geq T_{cld} \geq -60°C$. The top two panels (Figs. 9a,b) show CALIOP data at latitudes of >60°N, and the second row shows results for midlatitudes (30°–60°N). The CALIOP data in the Southern Hemisphere are similar to those in the Northern Hemisphere and are not shown. For CALIOP, the values of P_{11} fall within a narrow range from 0.28 to 0.34 with little dependence on cloud temperature. Values of P_{22}/P_{11} range from 0.35 to 0.5 with perhaps a slight tendency to increase with increasing cloud temperature. The lower four panels show results calculated from the microphysical data and associated single-scattering properties for the habit mixture. Results for smooth particles are not shown since the values for P_{11} are much larger than those for CALIOP, similar to those shown in the previous figure. For the nontropical habit mixture, the results for severely roughened particles tend to correspond more closely to the CALIOP data than do those for moderately roughened particles.

Results are shown in Fig. 10 using a habit mixture designed for deep tropical convective ice clouds (i.e., $T_{cld} \leq -55°C$). There is some overlap in cloud temperature with the results provided using the nontropical habit mixture. Solid columns are used instead of droxtals for the smallest particles in each PSD, and aggregates of plates are used according to Fig. 6c. The upper two panels show CALIOP data from 20°S to 20°N, with results obtained from the bulk scattering properties shown in the middle panels for moderately roughened particles and in the lowest panels for severely roughened particles. For deep tropical convection, the results obtained from the assumption of severely roughened particles correspond most closely to the CALIOP data.

5. Implications of the new models for MODIS

The use of a roughened particle has implications for other single-scattering properties. Figure 11 shows the

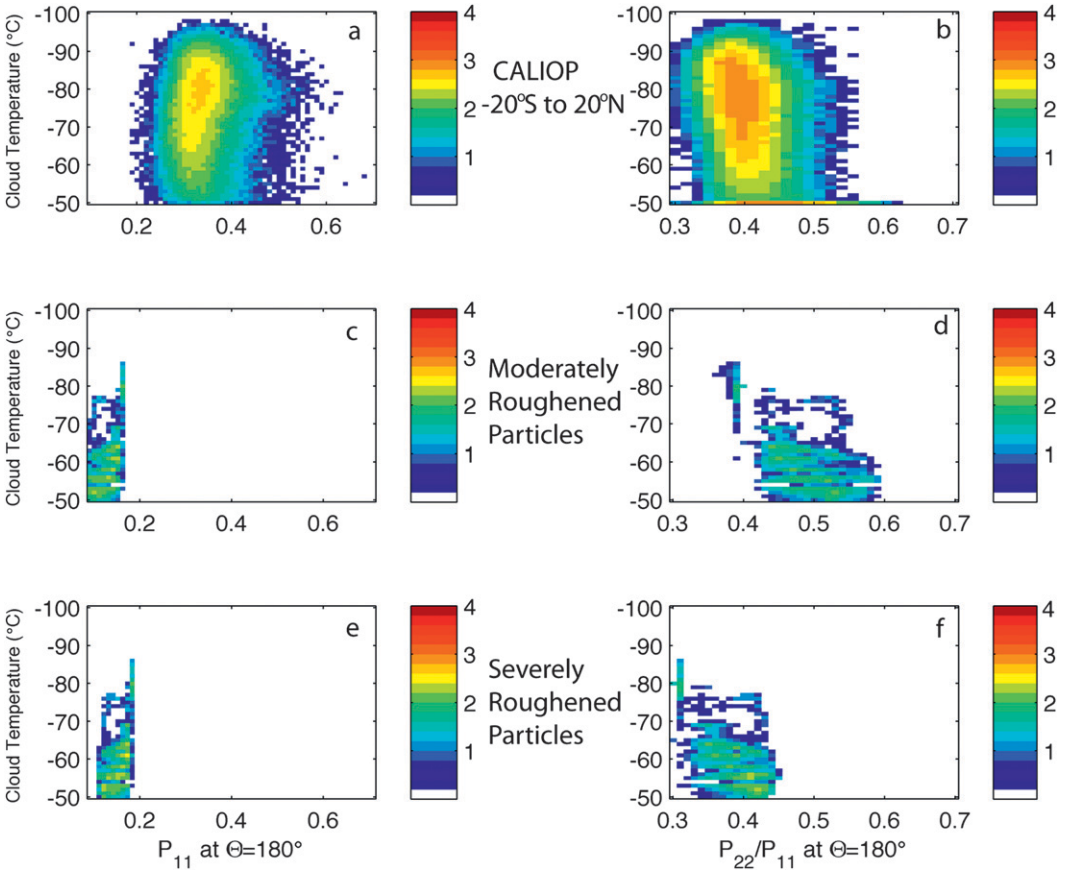

FIG. 10. As in Fig. 8, but for results that are based on the deep tropical convection habit mixture shown in Fig. 6c. The microphysical data are filtered for $T_{cld} \leq -55°C$.

asymmetry parameter at three wavelengths (0.65, 1.61, and 2.12 μm) and the single-scattering albedo at two of these wavelengths (1.61 and 2.12 μm) calculated for each of the 12 815 individual PSDs with the approach detailed in appendix B. Results are not shown for the single-scattering albedo at 0.65 μm since the value is unity (conservative scattering). Results are shown for the MODIS C5 model (gray symbols; assumes smooth particles for all habits except for a severely roughened aggregate of columns) and the generalized habit mixture (Fig. 6a) for moderately roughened (black symbols) and severely roughened particles. For the severely roughened particles, the individual points are color coded by field campaign to provide some guidance as to the source of the data. Although the single-scattering albedo is unaffected by particle roughening, the asymmetry parameter has a strong dependence on roughening. In general, the asymmetry parameter decreases with increasing particle surface roughness. For $D_{max} < 40$ μm, the asymmetry parameters for the C5 model and the moderately roughened particles are similar but diverge at larger sizes. For severely roughened particles, the asymmetry parameter is much lower than for the C5 and moderately roughened particles even at small D_{max}.

Several previous studies have shown that the ice-cloud optical thickness retrievals are sensitive to the value of the asymmetry parameter used in the algorithm. For example, Zhang et al. (2009) noted a >30% difference in ice-cloud optical thickness between the MODIS and POLDER cloud property products. The differences could be explained by the use of different ice-particle models (to be more specific, differing values of the asymmetry parameter) in the MODIS and POLDER ice-cloud retrieval algorithms.

Figures 12 and 13 show one way of ascertaining the changes that may be expected in inferred optical thickness τ and effective particle size D_{eff} between the MODIS C5 and roughened-particle models based on the generalized habit mixture shown in Fig. 6a. Figure 12 shows a lookup table (LUT) of reflectances as a function of τ and D_{eff} that are calculated for MODIS band 1 (0.65 μm) and band 7 (1.64 μm) assuming the C5 habit mixture (black lines) and the generalized habit mixture (red lines). Figure 12a assumes all

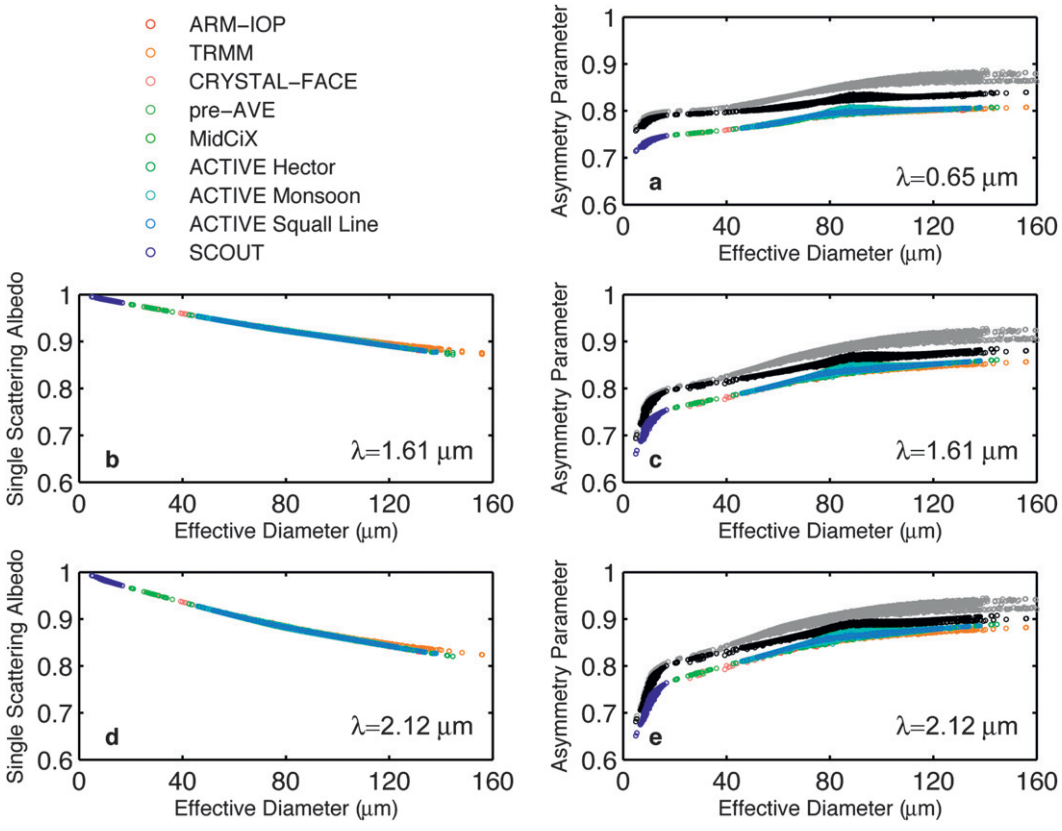

FIG. 11. (a) The asymmetry parameter as a function of effective diameter D_{eff} at a wavelength of 0.65 μm. Each point represents the value calculated for an individual PSD. Results in gray are obtained using the MODIS C5 habit distribution, and the results in black are obtained with the generalized habit distribution (Fig. 6a) assuming moderately roughened particles. The color-coded symbols represent results obtained using PSDs from a particular field campaign using the severely roughened particles. Also shown are results at 1.61 μm for (b) single-scattering albedo and (c) asymmetry parameter as a function of D_{eff}, with similar results shown in (d) and (e) at a wavelength of 2.12 μm. Note that values of the single-scattering albedo do not change with particle roughness.

particles are moderately roughened ($\sigma = 0.03$), and Fig. 12b shows results for severely roughened particles. Figure 13 shows similar results but for MODIS band 1 (0.65 μm) and band 7 (2.12 μm). The viewing geometry for this set of calculations assumes that the solar zenith and viewing zenith angles are 30°, respectively, and that the relative azimuth angle is 90°. The C5 models were rederived using the new single-scattering properties and microphysical data. In general, the two models provide similar reflectances for small D_{eff}, but the differences increase with increasing D_{eff}. The influence of the aggregate of plate particles is seen in that the 0.65-μm reflectances increase rather than decrease when $D_{\text{eff}} > 90$ μm. In comparison with C5, the tendency is that τ will decrease and D_{eff} will increase if moderately roughened particles are assumed. Figure 12b shows similar results but for the generalized habit mixture; severely roughened particles ($\sigma = 0.5$) are assumed. The differences between C5 and the new model in inferred τ and D_{eff} are more evident over the entire domain.

6. Summary

This study discusses the evolution in the development of bulk scattering/absorption models at solar wavelengths. As with the earlier model development, a combination of microphysical measurements from various field campaigns is combined with a library of individual ice-habit single-scattering properties to develop bulk scattering and absorption properties.

In this study, new microphysical measurements are now incorporated from a number of recent field campaigns in both the Northern and Southern Hemisphere. The number of particle size distributions available for use has increased by more than an order of magnitude since the earlier study (Baum et al. 2005a), from 1117 to 12 815, even when filtering the available data so that

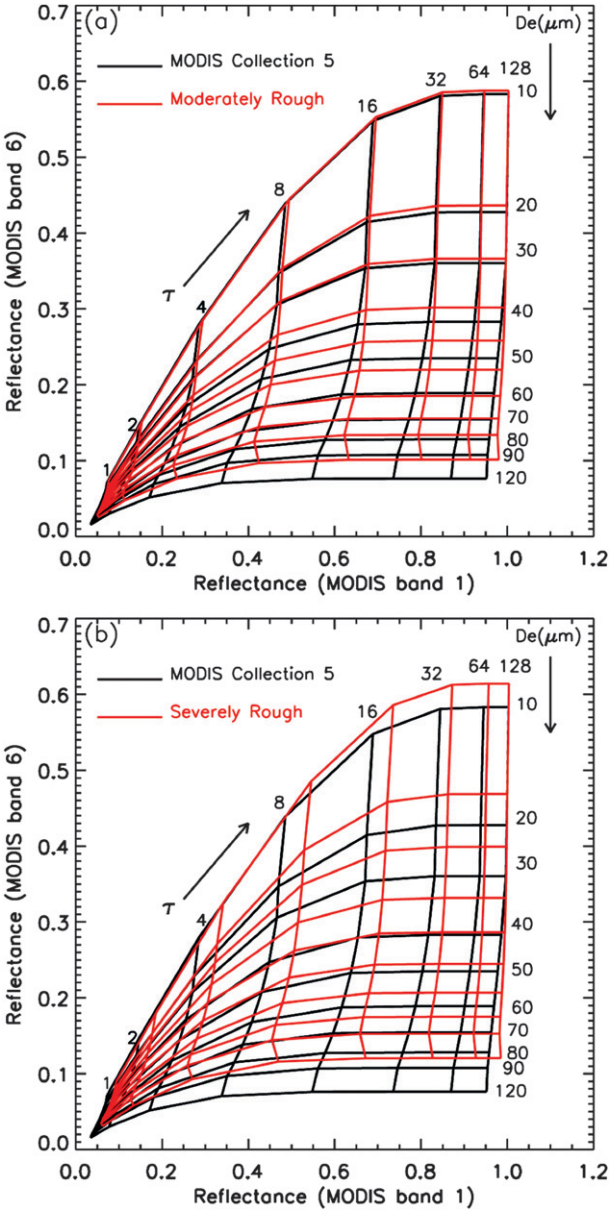

FIG. 12. Reflectances calculated for MODIS band 1 (0.65 μm) and band 6 (1.64 μm) for (a) MODIS C5 habit mixture (black lines; all particles are smooth except for the aggregate of columns) rederived using the new single-scattering properties and the generalized habit mixture (red lines) assuming all particles are moderately roughened ($\sigma = 0.03$) and for (b) MODIS C5 habit mixture (black lines) and the generalized habit mixture assuming all particles are severely roughened ($\sigma = 0.5$). The viewing geometry for this set of calculations assumes that the solar zenith and viewing zenith angles are both 30° and that the relative azimuth angle is 90°.

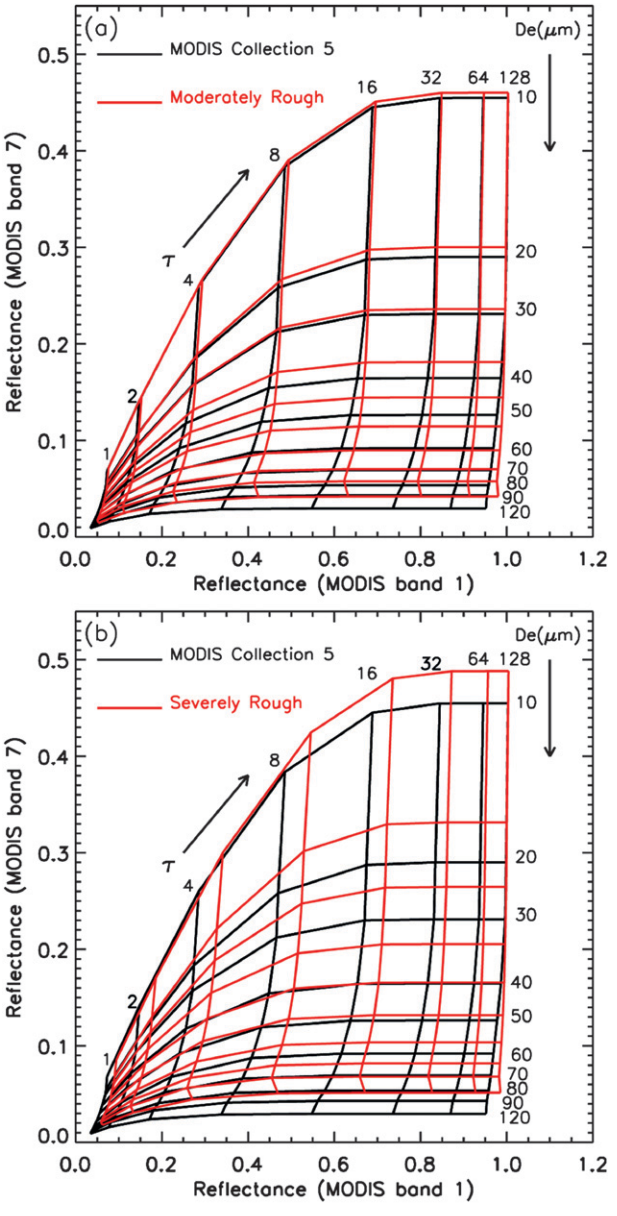

FIG. 13. As in Fig. 12, but for MODIS band 1 (0.65 μm) and band 7 (2.12 μm).

$T_{cld} \leq -40$°C. The IWC in the microphysical data now ranges from 10^{-6} to 10^{0} g m^{-3}, an increase of three orders of magnitude from the earlier study. Some of the PSDs now extend down to micrometer sizes (CRYSTAL-FACE, preAVE, and SCOUT). Based on these new data, it is now possible to build models for much lower D_{eff} values without artificially increasing the number of small particles. Furthermore, the microphysical data from the ARM, TRMM, and CRYSTAL-FACE campaigns in cold, optically thin ice clouds (rather than the warmer cloud data from the Citation) have been reprocessed to mitigate the shattering issue for the 2D probes as described by Field et al. (2006).

For evaluation purposes, a limited library of single-scattering properties is employed for 101 wavelengths

between 0.4 and 2.24 μm. The wavelengths were chosen to provide the spectral information necessary to build models for selected MODIS bands for testing prior to collection-6 software deliveries. The library includes the full phase matrix as well as properties for smooth, moderately roughened, and severely roughened particles ($\sigma = 0, 0.03$, and 0.5, respectively). In addition to the set of habits previously employed (droxtals, plates, hollow/solid columns, 3D solid bullet rosettes, and an aggregate of solid columns), three new habits have been incorporated: 3D hollow bullet rosettes and a small/large aggregate of plates. This additional information provides further complexity for building new models and also permits comparison with polarization measurements from sensors such as CALIOP.

On the basis of the updated microphysical data and libraries of single-scattering properties, three habit mixtures were developed. The first is a generalized habit mixture that involves all nine habits, the second is based on primarily midlatitude cirrus data, and the third is oriented toward tropical deep convective cirrus. Results were presented of the comparison of calculated median mass diameter D_m and IWC values with those inferred from the in situ microphysical measurements.

Of more interest was the additional constraint provided by the comparison with CALIOP data, specifically P_{11} and P_{22}/P_{11} at $\Theta = 180°$. For all habit mixtures, models developed using severely roughened particles tend to compare more closely to CALIOP backscattering measurements than do models built using less roughened particles. If smooth particles were assumed, the comparisons of the P_{11} component with the corresponding values from CALIOP were very different.

This study also compared the current set of models using the generalized habit distribution with the MODIS C5 models that assumed smooth particles except for the aggregate-of-columns habit. In a comparison of reflectances computed for MODIS band 1 (0.65 μm) and band 6 (1.64 μm) as well as for MODIS bands 1 and 7 (2.12 μm), it was shown that the inferred values of τ would decrease while D_{eff} would increase over those from MODIS C5 with use of the roughened particle models. In this comparison with C5, τ will decrease and D_{eff} will increase if either moderately or severely roughened particles are assumed. Given the strong influence of particle roughening on the inferred optical/microphysical characteristics for ice clouds, it will be important to continue to explore the use of polarization data in future development of bulk ice-cloud scattering and absorption models.

In future work, we will extend the development of single-scattering models to cover the wavelength range from 0.4 to 100 μm with no spectral gaps. The development of the library of single-scattering properties for the nine habits discussed herein is under way at the time of this writing. Based on these new spectral models, both narrowband (i.e., satellite imagers) and broadband models will be developed using consistent methods.

Acknowledgments. Bryan Baum, Andy Heymsfield, and Ping Yang gratefully acknowledge the support provided through NASA Grant NNX08AF81G and associated subcontracts to Texas A&M University and the National Center for Atmospheric Research through the University of Wisconsin—Madison. The authors appreciate many useful discussions with Dr. Steve Platnick of the NASA Goddard Space Flight Center and the invaluable insight offered by Dr. Anthony Baran at the Met Office in the United Kingdom. The effort on the single-scattering computations is partly supported by a research grant from NASA (NNX08AF68G) from the NASA Radiation Sciences Program managed by Dr. Hal Maring and the MODIS Program managed by Dr. Paula Bontempi.

APPENDIX A

Bulk Microphysical Properties

For a given PSD, the total projected area and total volume of ice per unit volume of air are given by

$$A_{\text{Tot}} = \sum_{h=1}^{M} \left[\int_{D_{\text{min}}}^{D_{\text{max}}} A_h(D) f_h(D) n(D)\, dD \right] \quad \text{and} \quad \text{(A1)}$$

$$V_{\text{Tot}} = \sum_{h=1}^{M} \left[\int_{D_{\text{min}}}^{D_{\text{max}}} V_h(D) f_h(D) n(D)\, dD \right], \quad \text{(A2)}$$

respectively, where D_{min} and D_{max} describe the minimum and maximum particle sizes in the distribution, $f_h(D)$ is the ice-particle habit fraction of habit h for size D, $n(D)$ is the number distribution for size D, and $A_h(D)$ and $V_h(D)$ are the area and volume of a specific particle of habit h for size D, respectively. The habit fraction is defined so that, for each size bin,

$$\sum_{h=1}^{M} f_h(D) = 1. \quad \text{(A3)}$$

The IWC for a given PSD is obtained by multiplying the total volume of ice by the bulk ice density (0.917 g cm^{-3}):

$$\mathrm{IWC} = \rho_{\mathrm{ice}} \sum_{h=1}^{M} \left[\int_{D_{\min}}^{D_{\max}} V_h(D) f_h(D) n(D)\, dD \right]. \quad \text{(A4)}$$

The effective diameter D_{eff} is proportional to the ratio of the total volume to the total projected area for a given particle size distribution and is defined as

$$D_{\mathrm{eff}} = \frac{3}{2} \frac{\sum_{h=1}^{M} \left[\int_{D_{\min}}^{D_{\max}} V_h(D) f_h(D) n(D)\, dD \right]}{\sum_{h=1}^{M} \left[\int_{D_{\min}}^{D_{\max}} A_h(D) f_h(D) n(D)\, dD \right]} = \frac{3}{2} \frac{V_{\mathrm{tot}}}{A_{\mathrm{tot}}}. \quad \text{(A5)}$$

APPENDIX B

Spectral Bulk Scattering Properties

This appendix provides the derivation of spectral bulk single-scattering properties following the approach discussed in Baum et al. (2005b, 2007). Here, the single-scattering properties are derived at an individual wavenumber rather than integrated over a spectral response function.

The mean scattering cross section at a specific wavenumber λ is given by

$$\overline{\sigma}_{\mathrm{sca}}(\lambda) = \frac{\int_{D_{\min}}^{D_{\max}} \left[\sum_{h=1}^{M} \sigma_{\mathrm{sca},h}(D,\lambda) f_h(D) \right] n(D)\, dD}{\int_{D_{\min}}^{D_{\max}} \left[\sum_{h=1}^{M} f_h(D) \right] n(D)\, dD}, \quad \text{(B1)}$$

where $\sigma_{\mathrm{sca},h}(D,\lambda)$ is the scattering cross section, M is the number of habits, D is particle size, and $n(D)$ is the particle density. The mean extinction cross section is given by

$$\overline{\sigma}_{\mathrm{ext}}(\lambda) = \frac{\int_{D_{\min}}^{D_{\max}} \left[\sum_{h=1}^{M} \sigma_{\mathrm{ext},h}(D,\lambda) f_h(D) \right] n(D)\, dD}{\int_{D_{\min}}^{D_{\max}} \left[\sum_{h=1}^{M} f_h(D) \right] n(D)\, dD}. \quad \text{(B2)}$$

The single-scattering albedo $\overline{\omega}$ is determined by the ratio of the mean scattering and extinction cross sections:

$$\overline{\omega}(\lambda) = \frac{\overline{\sigma}_{\mathrm{sca}}(\lambda)}{\overline{\sigma}_{\mathrm{ext}}(\lambda)}. \quad \text{(B3)}$$

The extinction efficiency Q_{ext} for a given particle size is the extinction cross section divided by the total projected area, and the mean extinction efficiency $\overline{Q}_{\mathrm{ext}}$ is the extinction cross section divided by the total projected area for a given particle size distribution:

$$\overline{Q}_{\mathrm{ext}}(\lambda) = \frac{\int_{D_{\min}}^{D_{\max}} \left[\sum_{h=1}^{M} Q_{\mathrm{ext},h}(D) A_h(D) f_h(D) \right] n(D)\, dD}{\int_{D_{\min}}^{D_{\max}} \left[\sum_{h=1}^{M} A_h(D) f_h(D) \right] n(D)\, dD}. \quad \text{(B4)}$$

The bulk extinction coefficient is defined as

$$\overline{\beta}_{\mathrm{ext}}(\lambda) = \int_{D_{\min}}^{D_{\max}} \left[\sum_{h=1}^{M} Q_{\mathrm{ext},h}(D,\lambda) A_h(D) f_h(D) \right] n(D)\, dD. \quad \text{(B5)}$$

As noted by Yang et al. (2001), for some applications it may be useful to define a volume-normalized extinction coefficient:

$$\tilde{\beta}_{\mathrm{ext}}(\lambda) = \frac{\overline{\beta}_{\mathrm{ext}}}{(\mathrm{IWC}/\rho_{\mathrm{ice}})} = \frac{\int_{D_{\min}}^{D_{\max}} \left[\sum_{h=1}^{M} Q_{\mathrm{ext},h}(D,\lambda) A_h(D) f_h(D) \right] n(D)\, dD}{\sum_{h=1}^{M} \left[\int_{D_{\min}}^{D_{\max}} V_h(D) f_h(D) n(D)\, dD \right]}. \quad \text{(B6)}$$

The scattering phase function $\overline{P}(\Theta)$ is given by

$$\overline{P}(\Theta,\lambda) = \frac{\int_{D_{\min}}^{D_{\max}} \left[\sum_{h=1}^{M} P_h(\Theta, D, \lambda)\, \sigma_{\mathrm{sca},h}(D,\lambda) f_h(D) \right] n(D)\, dD}{\int_{D_{\min}}^{D_{\max}} \left[\sum_{h=1}^{M} \sigma_{\mathrm{sca},h}(D,\lambda) f_h(D) \right] n(D)\, dD}, \quad \text{(B7)}$$

where Θ is the scattering angle.

The asymmetry factor $\overline{g}$ is provided by

$$\overline{g}(\lambda) = \frac{\int_{D_{\min}}^{D_{\max}} \left[\sum_{h=1}^{M} g_h(D,\lambda)\, \sigma_{\mathrm{sca},h}(D,\lambda) f_h(D) \right] n(D)\, dD}{\int_{D_{\min}}^{D_{\max}} \left[\sum_{h=1}^{M} \sigma_{\mathrm{sca},h}(D,\lambda) f_h(D) \right] n(D)\, dD}. \quad \text{(B8)}$$

APPENDIX C

Narrowband Bulk Scattering Properties

To build narrowband bulk single-scattering properties appropriate for an imager such as MODIS, the spectral single-scattering properties need to be integrated over a spectral response function. An example is provided for calculating the asymmetry factor (the other parameters are integrated similarly):

$$\langle \overline{g} \rangle = \frac{\int_{\lambda_{\min}}^{\lambda_{\max}} \overline{g}(\lambda) F_s(\lambda) S(\lambda)\, d\lambda}{\int_{\lambda_{\min}}^{\lambda_{\max}} F_s(\lambda) S(\lambda)\, d\lambda}, \tag{C1}$$

where $S(\lambda)$ is the solar spectrum and $F_s(\lambda)$ is the spectral response function. In this study, the solar spectrum used for integrating over the spectral response functions is given by Thuillier et al. (2003).

REFERENCES

Aumann, H. H., and Coauthors, 2003: AIRS/AMSU/HSB on the *Aqua* mission: Design, science objectives, data products, and processing systems. *IEEE Trans. Geosci. Remote Sens.,* **41,** 253–264.

Baran, A. J., 2009: A review of the light scattering properties of cirrus. *J. Quant. Spectrosc. Radiat. Transf.,* **110,** 1239–1260.

——, and L.-C. Labonnote, 2007: A self-consistent scattering model for cirrus. I: The solar region. *Quart. J. Roy. Meteor. Soc.,* **133,** 1899–1912.

——, P. N. Francis, L.-C. Labonnote, and M. Doutriaux-Boucher, 2001: A scattering phase function for ice cloud: Tests of applicability using aircraft and satellite multi-angle multi-wavelength radiance measurements of cirrus. *Quart. J. Roy. Meteor. Soc.,* **127,** 2395–2416.

Baum, B. A., A. J. Heymsfield, P. Yang, and S. T. Bedka, 2005a: Bulk scattering properties for the remote sensing of ice clouds. Part I: Microphysical data and models. *J. Appl. Meteor.,* **44,** 1885–1895.

——, P. Yang, A. J. Heymsfield, S. Platnick, M. D. King, and S. T. Bedka, 2005b: Bulk scattering properties for the remote sensing of ice clouds. Part II: Narrowband models. *J. Appl. Meteor.,* **44,** 1896–1911.

——, ——, S. L. Nasiri, A. J. Heidinger, A. J. Heymsfield, and J. Li, 2007: Bulk scattering properties for the remote sensing of ice clouds. Part III: High-resolution spectral models from 100 to 3250 cm^{-1}. *J. Appl. Meteor. Climatol.,* **46,** 423–434.

——, ——, Y.-X. Hu, and Q. Feng, 2010: The impact of ice particle roughness on the scattering phase matrix. *J. Quant. Spectrosc. Radiat. Transf.,* **111,** 2534–2549, doi:10.1016/j.jqsrt.2010.07.008.

Bi, L., P. Yang, G. Kattawar, B. A. Baum, Y.-X. Hu, D. M. Winker, R. S. Brock, and J. Q. Lu, 2009: Simulation of the color ratio associated with the backscattering of radiation by ice particles at 0.532 and 1.064 μm. *J. Geophys. Res.,* **114,** D00H08, doi:10.1029/2009JD011759.

de Reus, M., and Coauthors, 2009: Evidence for ice particles in the tropical stratosphere from in-situ measurements. *Atmos. Chem. Phys.,* **9,** 6775–6792.

Deschamps, P.-Y., F.-M. Breon, M. Leroy, A. Podaire, A. Brickaud, J.-C. Buriez, and G. Seze, 1994: The POLDER mission: Instrument characteristics and scientific objectives. *IEEE Trans. Geosci. Remote Sens.,* **32,** 598–615, doi:10.1109/36.297978.

Diner, D. J., and Coauthors, 1998: Multi-angle Imaging SpectroRadiometer (MISR) instrument description and experiment overview. *IEEE Trans. Geosci. Remote Sens.,* **36,** 1072–1087.

Evans, K. F., J. Wang, P. Racette, G. Heymsfield, and L. Li, 2005: Ice cloud retrievals and analysis with the compact scanning submillimeter imaging radiometer and the cloud radar system during CRYSTAL FACE. *J. Appl. Meteor.,* **44,** 839–859.

Field, P. R., A. J. Heymsfield, and A. Bansemer, 2006: Shattering and particle interarrival times measured by optical array probes in clouds. *J. Atmos. Oceanic Technol.,* **23,** 1357–1371.

Gosse, S., D. Labrie, and P. Chylek, 1995: Refractive index of ice in the 1.4–7.8-μm spectral range. *Appl. Opt.,* **34,** 6582–6586.

Heidinger, A. K., and M. J. Pavolonis, 2009: Gazing at cirrus clouds for 25 years through a split window. Part I: Methodology. *J. Appl. Meteor. Climatol.,* **48,** 1100–1116.

Heymsfield, A. J., 1986: Ice particles observed in a cirriform cloud at −83°C and implications for polar stratospheric clouds. *J. Atmos. Sci.,* **43,** 851–855.

——, and L. M. Miloshevich, 1995: Relative humidity and temperature influences on cirrus formation and evolution: Observations from wave clouds and FIRE II. *J. Atmos. Sci.,* **52,** 4302–4326.

——, S. Lewis, A. Bansemer, J. Iaquinta, L. M. Miloshevich, M. Kajikawa, C. Twohy, and M. R. Poellot, 2002: A general approach for deriving the properties of cirrus and stratiform ice cloud particles. *J. Atmos. Sci.,* **59,** 3–29.

——, C. G. Schmitt, A. Bansemer, and C. Twohy, 2010: Improved representations of ice particle masses based on observations in natural clouds. *J. Atmos. Sci.,* **67,** 3303–3318.

Hu, Y., 2007: Depolarization ratio–effective lidar ratio relation: Theoretical basis for space lidar cloud phase discrimination. *Geophys. Res. Lett.,* **34,** L11812, doi:10.1029/2007GL029584.

——, and Coauthors, 2007: The depolarization-attenuated backscatter relation: *CALIPSO* lidar measurements vs. theory. *Opt. Express,* **15,** 5327–5332.

——, and Coauthors, 2009: *CALIPSO*/CALIOP cloud phase discrimination algorithm. *J. Atmos. Oceanic Technol.,* **26,** 2293–2309.

Kindel, B. C., K. S. Schmidt, P. Pilewskie, B. A. Baum, P. Yang, and S. Platnick, 2010: Observations and modeling of cirrus shortwave spectral albedo during the Tropical Composition, Cloud and Climate Coupling Experiment. *J. Geophys. Res.,* **115,** D00J18, doi:10.1029/2009JD013127.

Labonnote, L.-C., G. Brogniez, J.-C. Buriez, M. Doutriaux-Boucher, J.-F. Gayet, and A. Macke, 2001: Polarized light scattering by inhomogeneous hexagonal monocrystals: Validation with ADEOS-POLDER measurements. *J. Geophys. Res.,* **106,** 12 139–12 154.

Liou, K. N., 1992: *Radiation and Cloud Processes in the Atmosphere—Theory, Observation, and Modeling*. Oxford University Press, 487 pp.

Mishchenko, M. I., J. W. Hovenier, and L. D. Travis, Eds., 2000: *Light Scattering by Nonspherical Particles: Theory, Measurements, and Applications*. Academic Press, 690 pp.

——, L. D. Travis, and A. A. Lacis, 2002: *Scattering, Absorption, and Emission of Light by Small Particles*. Cambridge University Press, 445 pp.

——, and Coauthors, 2007: Accurate monitoring of terrestrial aerosols and total solar irradiance: Introducing the Glory mission. *Bull. Amer. Meteor. Soc.,* **88,** 677–691.

Mitchell, D. L., W. P. Arnott, C. Schmitt, A. J. Baran, S. Havemann, and Q. Fu, 2001: Contributions of photon tunneling to extinction in laboratory grown hexagonal columns. *J. Quant. Spectrosc. Radiat. Transf.,* **70,** 761–776.

Platnick, S., M. D. King, S. A. Ackerman, W. Paul Menzel, B. A. Baum, and R. A. Frey, 2003: The MODIS cloud products: Algorithms and examples from *Terra*. *IEEE Trans. Geosci. Remote Sens.,* **41,** 459–473.

Platt, C. M. R., 1979: Remote sounding of high clouds: I. Calculation of visible and infrared optical properties from lidar and radiometer measurements. *J. Appl. Meteor.,* **18,** 1130–1143.

——, and A. C. Dilley, 1981: Remote sounding of high clouds. IV: Observed temperature variations in cirrus optical properties. *J. Atmos. Sci.,* **38,** 1069–1082.

Schmitt, C. G., and A. J. Heymsfield, 2007: On the occurrence of hollow bullet rosette– and column-shaped ice crystals in midlatitude cirrus. *J. Atmos. Sci.,* **64,** 4514–4519.

——, and ——, 2010: The dimensional characteristics of ice crystal aggregates from fractal geometry. *J. Atmos. Sci.,* **67,** 1605–1616.

——, J. Iaquinta, and A. J. Heymsfield, 2006: The asymmetry parameter of cirrus clouds composed of hollow bullet rosette–shaped ice crystals from ray-tracing calculations. *J. Appl. Meteor. Climatol.,* **45,** 973–981.

Thuillier, G., M. Hersé, D. Labs, T. Foujols, W. Peetermans, D. Gillotay, P. C. Simon, and H. Mandel, 2003: The solar spectral irradiance from 200 to 2400 nm as measured by the SOLSPEC spectrometer from the ATLAS 1-2-3 and EURECA missions. *Sol. Phys.,* **214,** 1–22.

Um, J., and G. M. McFarquhar, 2007: Single-scattering properties of aggregates of bullet rosettes in cirrus. *J. Appl. Meteor. Climatol.,* **46,** 757–775.

——, and ——, 2009: Single-scattering properties of aggregates of plates. *Quart. J. Roy. Meteor. Soc.,* **135,** 291–304.

Warren, S. G., 1984: Optical constants of ice from the ultraviolet to the microwave. *Appl. Opt.,* **23,** 1206–1225.

——, and R. E. Brandt, 2008: Optical constants of ice from the ultraviolet to the microwave: A revised compilation. *J. Geophys. Res.,* **113,** D14220, doi:10.1029/2007JD009744.

Westbrook, C. D., R. C. Ball, P. R. Field, and A. J. Heymsfield, 2004: Theory of growth by differential sedimentation, with application to snowflake formation. *Phys. Rev. E,* **70,** 021403, doi:10.1103/PhysRevE.70.021403.

Winker, D. M., and Coauthors, 2010: The *CALIPSO* mission: A global 3D view of aerosols and clouds. *Bull. Amer. Meteor. Soc.,* **91,** 1211–1229.

Xie, Y., P. Yang, G. W. Kattawar, B. A. Baum, Y.-X. Hu, 2011: On the scattering properties of ice particle aggregates for the remote sensing of ice clouds. *Appl. Opt.,* **50,** 1065–1081.

Yang, P., K. N. Liou, K. Wyser, and D. Mitchell, 2000: Parameterization of the scattering and absorption properties of individual ice crystals. *J. Geophys. Res.,* **105,** 4699–4718.

——, B.-C. Gao, B. A. Baum, Y. X. Hu, W. J. Wiscombe, S.-C. Tsay, D. M. Winker, and S. L. Nasiri, 2001: Radiative properties of cirrus clouds in the infrared (8–13 μm). *J. Quant. Spectrosc. Radiat. Transf.,* **70,** 473–504.

——, B. A. Baum, A. J. Heymsfield, Y. X. Hu, H.-L. Huang, S.-C. Tsay, and S. Ackerman, 2003: Single-scattering properties of droxtals. *J. Quant. Spectrosc. Radiat. Transf.,* **79-80,** 1159–1169.

——, L. Zhang, G. Hong, S. L. Nasiri, B. A. Baum, H.-L. Huang, M. D. King, and S. Platnick, 2007: Differences between collection 4 and 5 MODIS ice cloud optical/microphysical products and their impact on radiative forcing simulations. *IEEE Trans. Geosci. Remote Sens.,* **45,** 2886–2899.

——, G. W. Kattawar, G. Hong, P. Minnis, and Y. Hu, 2008a: Uncertainties associated with the surface texture of ice particles in satellite-based retrieval of cirrus clouds. Part I: Single-scattering properties of ice crystals with surface roughness. *IEEE Trans. Geosci. Remote Sens.,* **46,** 1940–1947.

——, and Coauthors, 2008b: Effect of cavities on the optical properties of bullet rosettes: Implications for active and passive remote sensing of ice cloud properties. *J. Appl. Meteor. Climatol.,* **47,** 2311–2330.

Zhang, Z., P. Yang, G. W. Kattawar, S.-C. Tsay, B. A. Baum, Y. X. Hu, A. J. Heymsfield, and J. Reichardt, 2004: Geometrical-optics solution to light scattering by droxtal ice crystals. *Appl. Opt.,* **43,** 2490–2499.

——, ——, ——, J. Riedi, L.-C. Labonnote, B. A. Baum, S. Platnick, and H. L. Huang, 2009: Influence of ice particle model on satellite ice cloud retrieval: Lessons learned from MODIS and POLDER cloud product comparison. *Atmos. Chem. Phys.,* **9,** 7115–7129.